Carbon 243 (2025) 120593

Contents lists available at ScienceDirect

Carbon

journal homepage: www.elsevier.com/locate/carbon

Flash-Joule-heating enhancing electromagnetic absorption performance of cobalt polyphthalocyanine complex derived 2D Co/C nanocomposite

Tiancong Hao [a,b,1], Yuhang Liu [c,1], Wenyu Li [a], Xiaoning Yang [a,*], Xiongfei Liu [e], Qingya Sun [a,**], Shifei Tao [d], Aming Xie [a,***], Guowei Ma [e]

[a] School of Safety Science and Engineering, Nanjing University of Science and Technology, Nanjing, 210094, China
[b] School of Mechanical Engineering, Nanjing University of Science & Technology, Nanjing, 210094, China
[c] School of Materials Science and Engineering, Nanjing University of Science and Technology, Nanjing, 210094, China
[d] School of Electronic Engineering and Optoelectronic Technology, Nanjing University of Science and Technology, Nanjing, 210094, China
[e] School of Civil and Transportation Engineering, Hebei University of Technology, Tianjin, 300401, China

ARTICLE INFO

Keywords:
Flash Joule heating
Electromagnetic absorption
Carbon nanocomposite
Cobalt phthalocyanine

ABSTRACT

Conventional carbonization methodologies employed in the synthesis of carbon-based nanocomposites are frequently compromised by structural imperfections, which substantially diminish electromagnetic wave attenuation capabilities. To address this limitation, we herein propose a Flash-Joule-Heating (FJH) treatment strategy for microstructural refinement of 2D Co/C nanocomposite. After FJH treatment, it is revealed that the graphitization, structural ordering, and crystallinity improve remarkably. The obtained Co/C nanocomposite shows apparently enhanced electromagnetic waves absorption (EMA), where the effective absorption bandwidth broadens from 5 GHz to 6.12 GHz (a 22.4 % increase), compared to the untreated sample. The enhancing mechanism is predominantly attributed to the rebalancing of dielectric loss and a transition in the magnetic loss mechanism. This work demonstrates an effective treatment strategy for improving the microstructure and electromagnetic response of carbon-based nanocomposite, offering valuable insights into the design of high-performance EMA materials.

1. Introduction

With the rapid development of wireless communication, radar detection, and electromagnetic interference shielding technologies, high performance electromagnetic wave absorbing (EMA) materials have attracted increasing attention in both military and civilian applications [1–4]. To date, a wide range of absorptive materials have been explored, including magnetic metal oxides, MXenes, and carbon-based composite. Among them, carbon-based materials stand out due to their low density, high electrical conductivity, rich structural tunability, and ease of compositing with magnetic phases, making them ideal candidates for achieving lightweight, broadband, and efficient EMA performance [5–12]. Among carbon precursors, phthalocyanines have emerged as promising carbon precursors due to their excellent thermal stability and high carbon yield. When coordinated with transition metals, metal phthalocyanine complexes can simultaneously provide both carbon and magnetic phases during thermal treatment, enabling the construction of carbon-based absorbers with integrated dielectric and magnetic loss mechanisms [13–16].

In the development of carbon-based absorbers, conventional thermal treatment methods, including hydrothermal synthesis and tube furnace carbonization, have been widely adopted to tailor structural and electromagnetic properties [17–19]. However, hydrothermal processes typically occur at low temperatures and yield poorly conductive materials with limited graphitization. Tube furnace carbonization, although capable of producing graphitic carbon, often involves prolonged treatment, uncontrolled particle agglomeration, and limited defect regulation [20,21]. These drawbacks hinder the construction of conductive networks, interfacial polarization centers, and controlled defect states which are essential for both dielectric and magnetic loss mechanisms in

* Corresponding author.
** Corresponding author.
*** Corresponding author.
E-mail addresses: Xiaoninghht@163.com (X. Yang), qingyasun@sina.com (Q. Sun), xieaming@njust.edu.cn (A. Xie).
[1] These authors contributed equally to this work.

https://doi.org/10.1016/j.carbon.2025.120593
Received 12 May 2025; Received in revised form 24 June 2025; Accepted 2 July 2025
Available online 2 July 2025

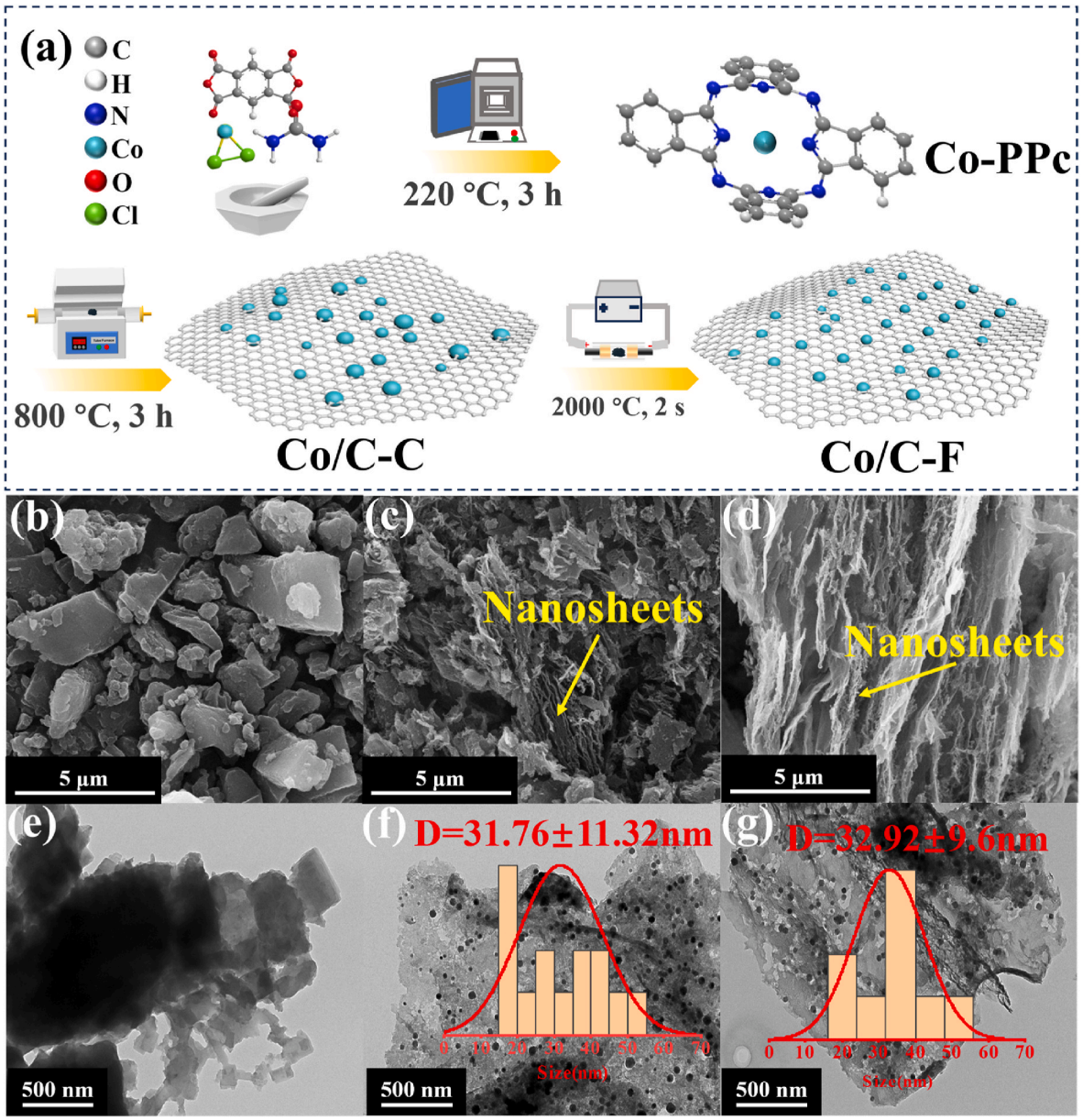

Fig. 1. (a) Schematic preparation of Co/C nanocomposite; SEM images of (b) Co-PPc, (c) Co/C–C, and (d) Co/C–F; TEM images and size distribution of (e) Co-PPc, (f) Co/C–C, and (g) Co/C–F.

electromagnetic wave absorption [22–25]. To address these limitations, advanced thermal strategies such as ultrahigh-temperature annealing (>2000 °C) and arc-discharge processing have been explored for further enhancing graphitization and optimizing microstructures. Nevertheless, these methods are costly, energy-intensive, and still struggle to precisely control local structure or defect distribution. In contrast, Flash-Joule-Heating (FJH) has emerged as a highly efficient post-synthetic approach, offering ultrafast heating rates (10^4–10^5 K/s), low energy consumption, and precise thermal modulation through localized gradients. These features enable FJH to promote graphitization, inhibit agglomeration, and introduce structural defects within milliseconds [26]. Recent studies have applied FJH to carbon nanomaterials for supercapacitors, electrocatalysis, and electromagnetic absorption. However, most FJH applications have focused on 3D materials, while its effect on 2D carbon architecture remains underexplored [27–34].

In this work, we investigate the impact of FJH post-treatment on the electromagnetic absorption properties of 2D carbon nanocomposite, which was prepared from the cobalt polyphthalocyanine (Co-PPc) precursors [35–40]. Through systematic comparative analysis between tube furnace carbonization alone and tube furnace carbonization followed by FJH processing, the structural and functional advantages conferred by FJH are elucidated. The findings provide new insights into post-processing strategies for optimizing carbon nanostructures in advanced electromagnetic applications.

2. Experimental section

2.1. Materials

Pyromellitic dianhydride (PMDA), $CoCl_2{\cdot}6H_2O$, NH_4Cl, $(NH_4)_6Mo_7O_{24}{\cdot}4H_2O$, urea, and other chemical reagents were obtained from commercial suppliers. All reagents were of analytical grade and were used without further purification.

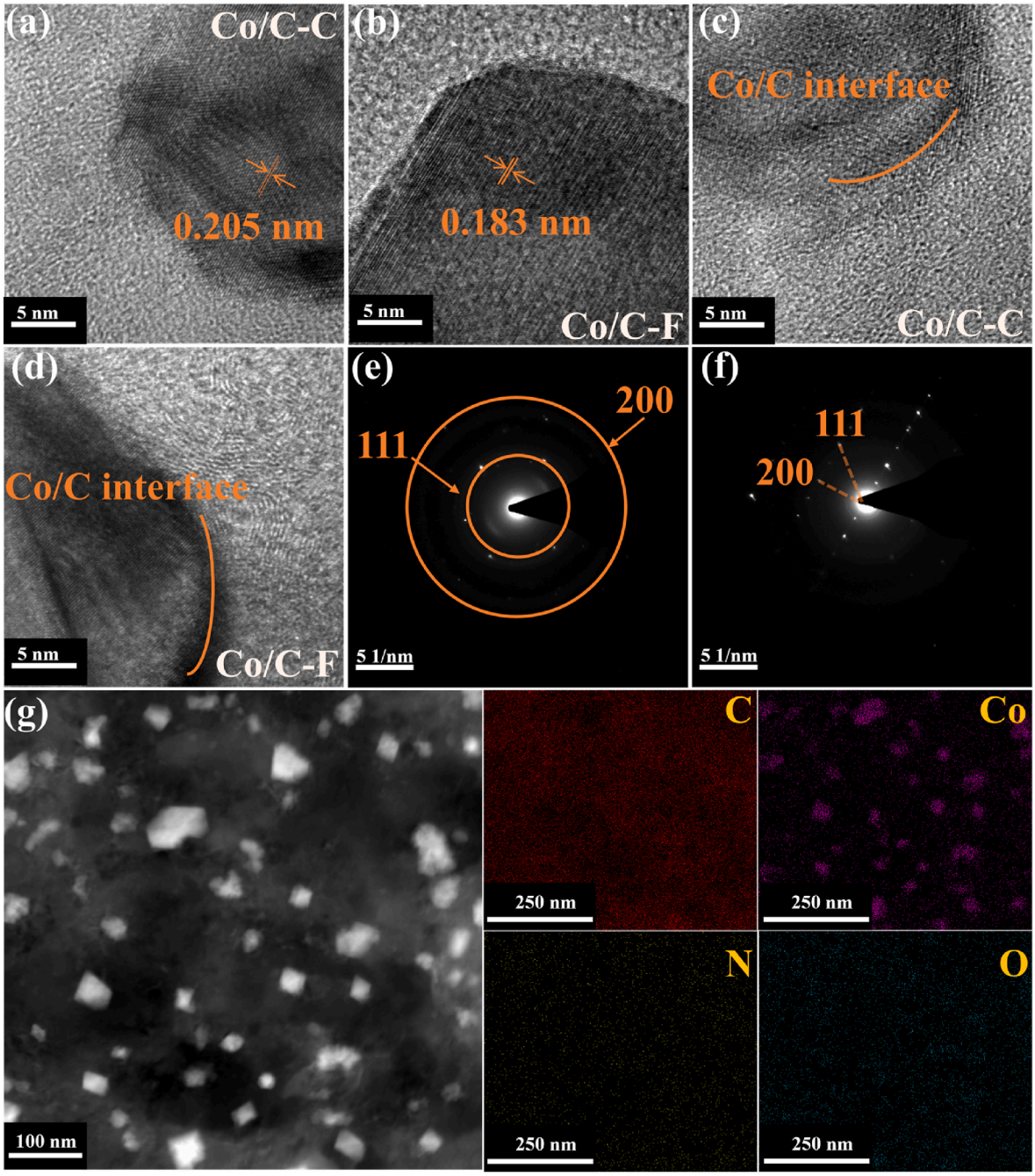

Fig. 2. (a–d) HRTEM images, SAED pattern of (e) Co/C–C, (f) Co/C–F; (g) HAADF-STEM image and the elemental mappings of Co/C–F.

2.2. Synthesis of Co-PPc precursors

The Co-PPc precursor was synthesized via a modified solid-state reaction methodology. PMDA (4.8 mmol, 1.05 g), $CoCl_2{\cdot}6H_2O$ (2.3 mmol, 0.548 g), urea (34.1 mmol, 2.05 g), NH_4Cl (9.4 mmol, 0.5 g), and $(NH_4)_6Mo_7O_{24}{\cdot}4H_2O$ (1.8 μmol, 0.00225 g) were thoroughly ground together to ensure homogeneity. The resulting mixture was subsequently transferred into a quartz boat and heated at 220 °C for 3 h in a muffle furnace. Following natural cooling to room temperature, the obtained powder was washed three times with deionized water and ethanol to remove residual impurities. The sample was then dried under vacuum conditions at 70 °C for 12 h, yielding the Co-PPc precursor.

2.3. The synthesis of nanocomposite

For Co/C nanocomposite preparation, Co-PPc precursor was first subjected to controlled carbonization at 800 °C for 3 h in a tube furnace under an argon atmosphere, followed by FJH treatment at 2000 °C for 2 s under vacuum conditions to obtain the final product.

3. Results and discussions

The synthesis of Co/C nanocomposites follows a sequential thermal process route (Fig. 1a). Co-PPc, representing Co-PPc precursors, is prepared through solid-state reactions involving PMDA, $CoCl_2{\cdot}6H_2O$, urea, NH_4Cl, and $(NH_4)_6Mo_7O_{24}{\cdot}4H_2O$. Then Co-PPc is carbonized at 800 °C for 3 h in an argon environment to generate Co/C–C. The resulting material is further processed by FJH at 2000 °C for 2 s under vacuum to

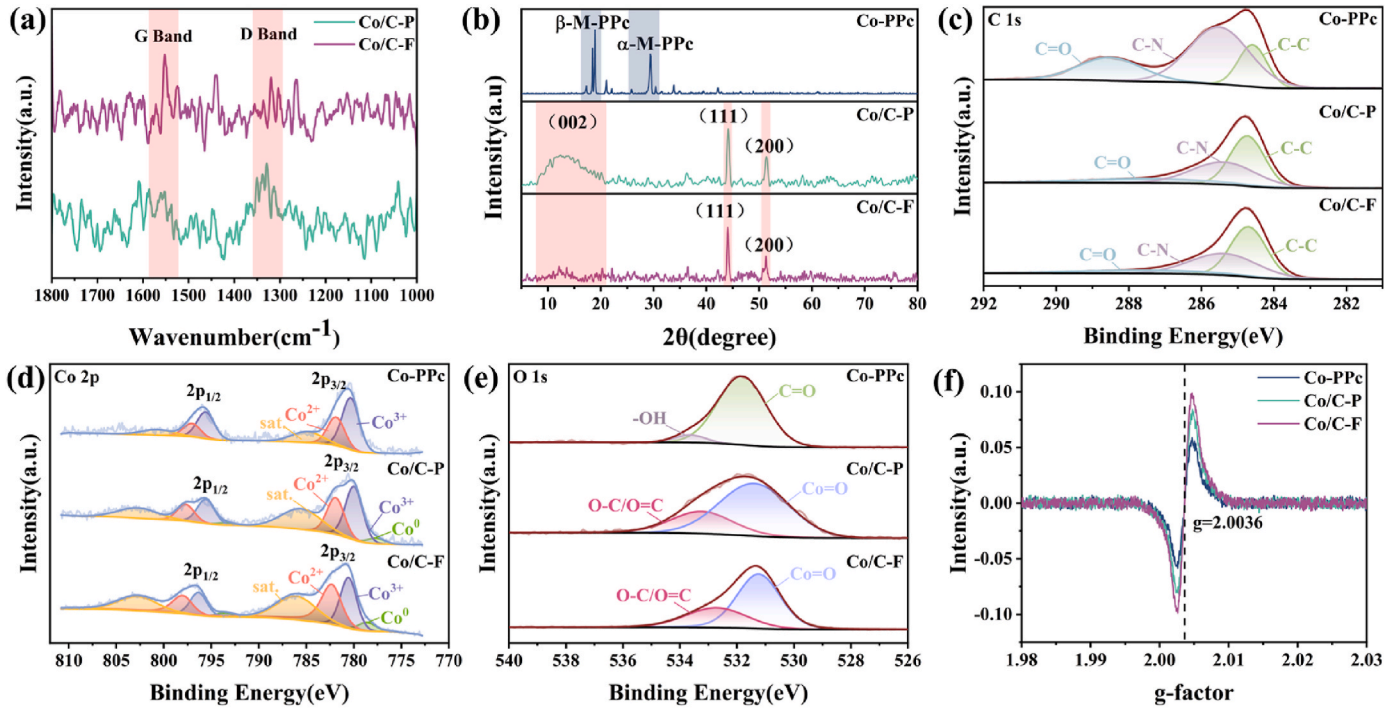

Fig. 3. (a) Raman spectra, (b) XRD patterns; The high-resolution XPS spectra of (c) C 1s, (d) Co 2p, and (e) O 1s; (f) EPR spectra.

obtain Co/C–F. Fig. 1b–e and S1 show the influence of treatment on the morphology of Co/C nanocomposite. Co-PPc shows a distinctive scattered blocky morphology, with dimensions ranging from several hundred nanometers to micrometers. The particles exhibit rough surface textures and irregular edge formations. Co/C-2 carbonized at 800 °C displays well-defined layered sheet structures (Fig. 1c). Higher magnification analysis reveals the emergence of nanoparticles distributed on the surface with a grain size distribution of 31.76 ± 11.32 nm, accompanied by regions of graphitization; additionally, notable aggregation is also observed (Fig. 1f). Co/C–F exhibits enhanced graphitization with pronounced layered sheet formation and a more uniform distribution of particles with a refined grain size distribution of 32.92 ± 9.6 nm, suggesting partial mitigation of aggregation (Fig. 1d–g). Although the average grain size remains similar, the standard deviation significantly decreases, indicating that FJH effectively regulates the particle size distribution, making it more uniform.

The random nanoparticles of Co/C–C and Co/C–F are shown in Fig. 2a and b and S2. For Co/C–C, clear lattice fringes with a spacing of 0.205 nm are visible, corresponding to the (111) crystal plane of face-centered cubic (fcc) Co. In the case of Co/C–F, the lattice fringes become more compact and well-defined, with a reduced spacing of 0.183 nm, corresponding to the (200) plane of fcc Co. These observations confirm the presence of crystalline Co domains in both samples which may contribute to enhanced dielectric and magnetic loss in the composite. Co nanoparticles are encapsulated within carbon matrices in both samples, forming Co@C core-shell structures (Fig. 2c and d). The carbon shells in Co/C–C are disordered with loosely arranged layers, while Co/C–F exhibits enhanced carbon ordering with continuous, well-defined shells. The carbon fringes transform from fragmented, dot-like patterns in Co/C–C to well-developed, arc-shaped structures in Co/C–F. This enhanced structural organization suggests that the FJH treatment promotes rapid reorganization of the carbon matrix, resulting in more ordered interfacial structures. The selected area electron diffraction (SAED) patterns of Co/C–C and Co/C–F reveal distinct crystalline characteristics (Fig. 2e and f). Co/C–C exhibits continuous ring-like diffraction patterns, indicating typical polycrystalline structure with randomly oriented small Co grains. In contrast, Co/C–F displays a clear spot diffraction pattern with discrete, bright diffraction spots arranged in regular lattice configurations, characteristic of single-crystalline or large-grained structures with preferred orientation. This transformation from ring to spot patterns demonstrates that FJH treatment significantly improves the crystallinity and structural ordering of the metallic Co phase. HAADF-STEM image reveals numerous bright spots corresponding to uniformly distributed high-density nanoparticles in the Co/C–F (Fig. 2g). The elemental mapping confirms that Co is predominantly concentrated in these bright regions, while carbon and nitrogen are homogeneously distributed throughout the matrix, establishing a continuous N-doped carbon framework. Notably, nitrogen exhibits localized enrichment around Co nanoparticles, suggesting potential Co-N_x coordination formation that may modulate the electronic structure. Oxygen displays uniform but weak distribution. In contrast, Co/C–C shows larger Co nanoparticles with partial agglomeration, less homogeneous carbon/nitrogen matrix distribution, and stronger oxygen signals (Fig. S3).

In the Raman spectra (Fig. 3a), Co/C–C exhibits a high I_D/I_G ratio of 1.82, indicating a disordered carbon framework with dense defects and an amorphous-dominated structure. In contrast, the sample after FJH treatment shows a much lower I_D/I_G ratio of 0.61, suggesting reduced defect density and improved graphitization. These results confirm that FJH facilitates structural reordering and the formation of a more ordered carbon network, which promotes the development of conductive pathways and enhances conductive loss, thereby improving electromagnetic wave attenuation performance. It is evident from Fig. 3b that the XRD pattern of Co-PPc can be deconvoluted into two typical π-π stacking polymorphs corresponding to metal phthalocyanines: the uniformly stacked α-phase (α-M-PPc) and the staggered β-phase (β-M-PPc). Diffraction peaks observed at 2θ = 17.3°, 18.5°, and 18.9° correspond to the (200), (001), and (101) planes of β-M-PPc, while the signals at 25.8°, 29.4°, and 30.4° can be indexed to the (310), (001), and (101) planes of α-M-PPc. In the XRD patterns of Co/C–C and Co/C–F, pronounced peaks appear at 2θ ≈ 44.12° and 51.38°, which can be assigned to the (111) and (200) planes of face-centered cubic metallic cobalt. This indicates that partial reduction of Co species occurred during thermal treatment, leading to the formation of crystalline metallic Co. In addition, Co/C–C

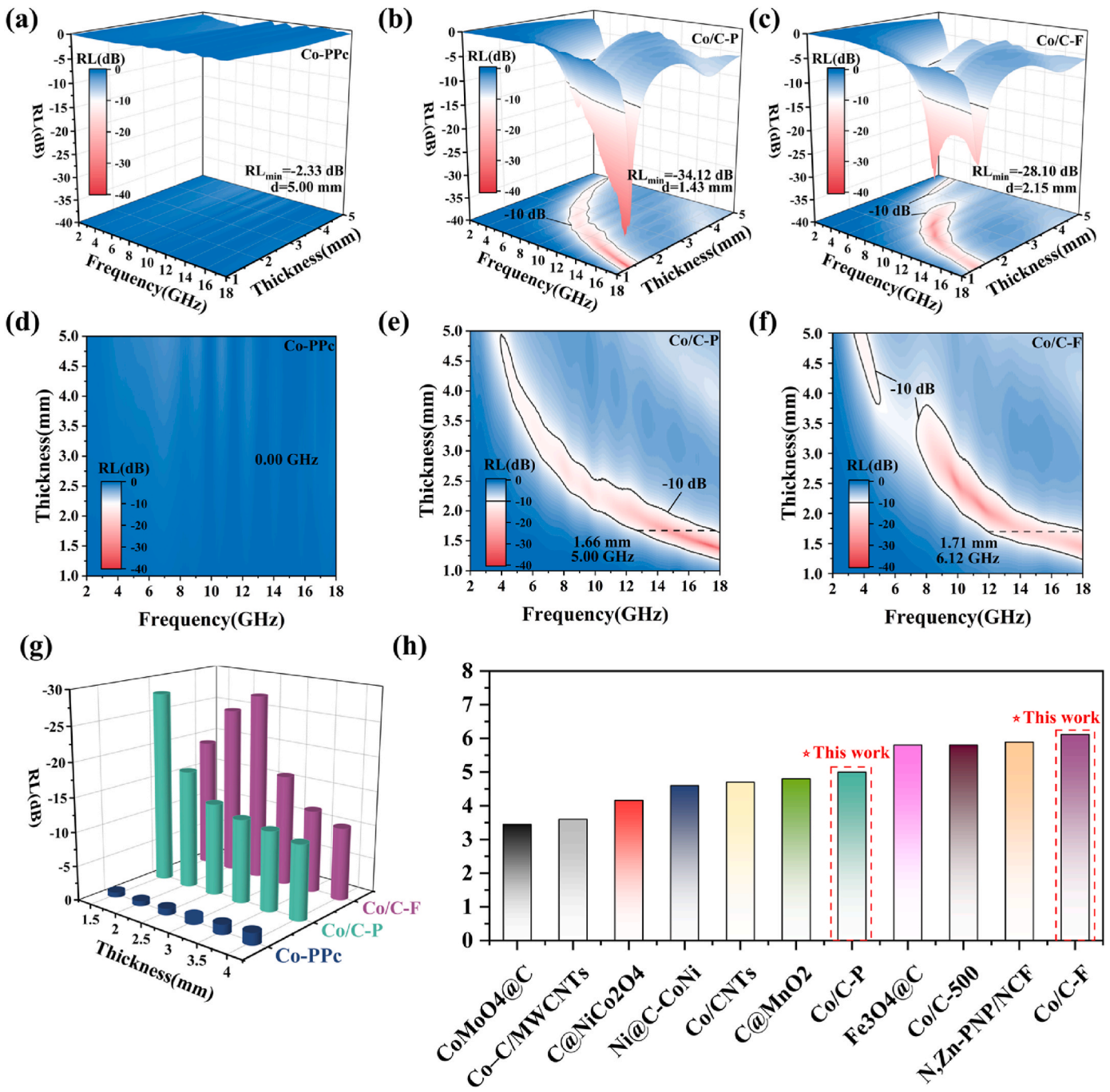

Fig. 4. 3D RL curves of (a) Co-PPc, (b) Co/C–C, and (c) Co/C–F; corresponding 2D diagrams of (d) Co-PPc, (e) Co/C–C, and (f) Co/C–F; (g) RL histogram distribution of Co-PPc, and (h) Comparison graph of EMW absorption performance

exhibits a broad and weak diffraction band in the 2θ range of 7.8°–21.0°, centered at approximately 12.4°, which corresponds to the (002) plane of amorphous carbon with an interlayer spacing of ~7.13 Å, significantly larger than that of ideal graphite (3.35 Å). This suggests a highly disordered carbon stacking with a wide distribution of interlayer spacings. In contrast, after FJH the (002) peak becomes noticeably narrower and slightly shifts toward higher angles, indicating a contraction in interlayer distance and improved stacking order. These changes suggest that the carbon framework undergoes a transformation from a disordered to a locally ordered structure upon FJH, reflecting a clear trend toward graphitization.

X-ray Photoelectron Spectroscopy (XPS) analysis, as shown in Fig. 3 and S4, was carried out to examine the elemental distribution and chemical bonding environments in the samples [22,35,36,41,42]. Significant compositional changes are observed following carbonization, while the FJH treatment does not alter the elemental species present but instead adjusts their relative proportions. The high-resolution spectra further reveal the evolution of bonding environments for C, N, Co, and O. In the C 1s region, Co-PPc exhibits dominant C–N (285.5 eV) and C═O (288.6 eV) peaks, along with a relatively weak C–C signal at 284.6 eV (Fig. 3c). After carbonization, the C–C component increases markedly, while C–N and C═O intensities decrease; this trend continues in Co/C–F, where heteroatom-related peaks are further suppressed and the C–C signal remains prominent. In the Co 2p spectra (Fig. 3d), Co-PPc shows peaks for Co^{3+} (780.4 eV), Co^{2+} (781.9 eV), and a satellite at 785.0 eV. Following carbonization, a Co^{0} peak emerges at 777.7 eV,

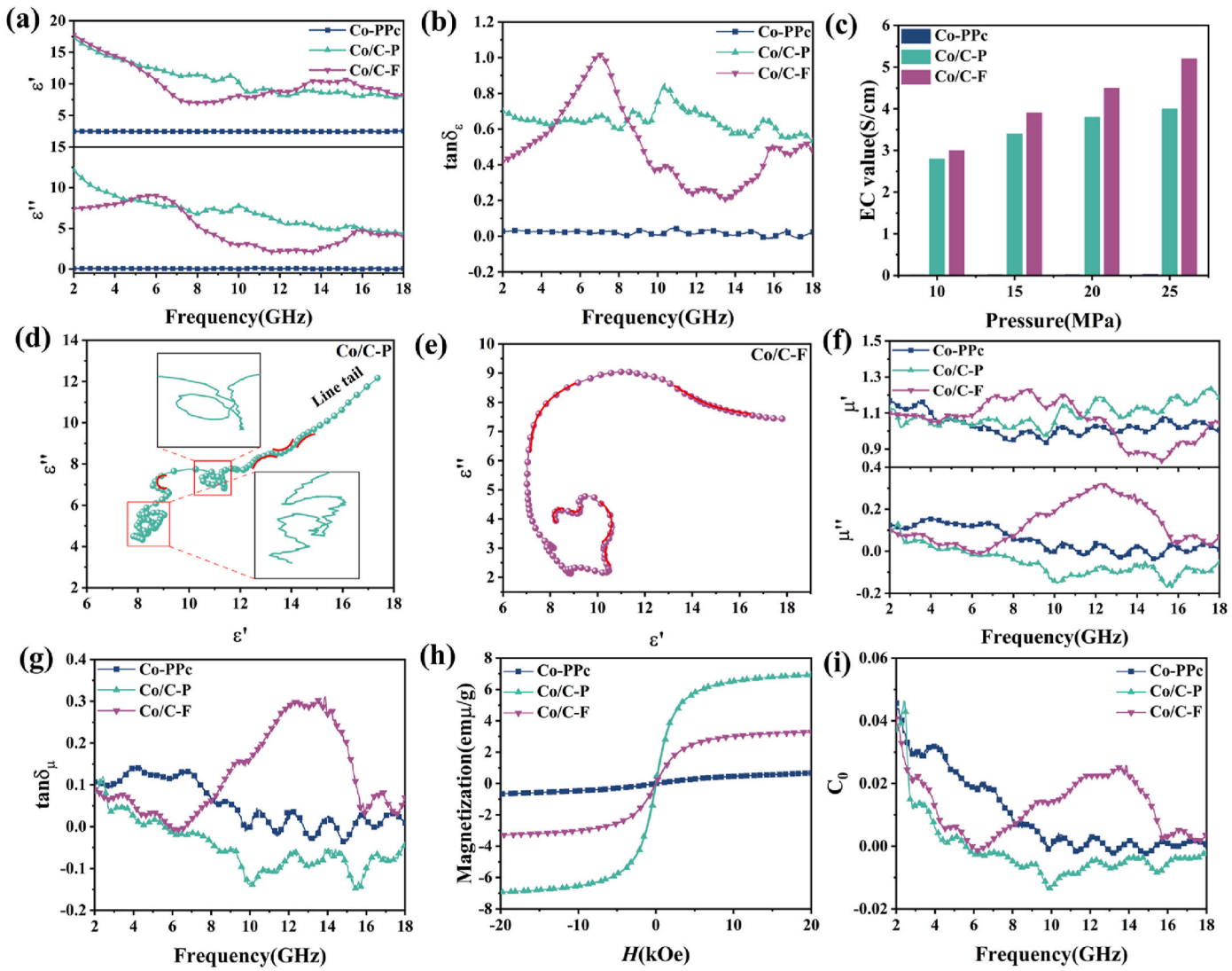

Fig. 5. Electromagnetic parameters of Co/C: (a) ε_r, (b) tan δ_ε, (c) Conductivity of Co/C, (d) Cole-Cole graphs of Co/C–C, (e) Cole-Cole graphs of Co/C–F, (f) μ_r, (g) tan δ_μ, (h) hysteresis loops, (i) C_0-f curve.

accompanied by Co^{3+} and Co^{2+}, and a shifted satellite at 785.8 eV. In Co/C–F, the Co^0 signal becomes more intense (778.6 eV), the oxidized states persist (780.6 and 782.4 eV), and the satellite further shifts to 786.2 eV. The N 1s spectra (Fig. S4b) of Co-PPc contains three components: pyridinic N (398.9 eV), pyrrolic N (400.2 eV), and Co–N (401.1 eV). After carbonization, the pyrrolic and Co–N components disappear, while pyridinic N (398.4 eV) remains and graphitic N (400.8 eV) emerges. In Co/C–F, both nitrogen species exhibit slight shifts to lower binding energies (398.2 and 400.5 eV), indicating subtle changes in the local electronic environment. In the O 1s spectra, Co-PPc mainly shows C═O (531.8 eV) and –OH (533.7 eV). After carbonization, a Co–O component appears at 531.4 eV and the O–C/O═C peak shifts to 533.3 eV; after FJH, the Co–O peak becomes sharper and shifts to 531.2 eV, while the O–C/O═C signal slightly decreases to 532.7 eV. Compared with the carbonized sample, the FJH-treated material demonstrates a more graphitized carbon framework, higher metallic cobalt content, improved coordination uniformity, and stabilized nitrogen species. These structural advantages are expected to enhance electrical conductivity, increase dipolar polarization strength, and collectively contribute to the electromagnetic wave absorption performance. EPR analysis shows that the FJH-treated sample exhibits the strongest paramagnetic signal, indicating the highest concentration of defect-related unpaired electrons (Fig. 3f). This result, while seemingly inconsistent with the enhanced graphitization observed in Raman and XRD, is attributed to the formation of abundant interfacial defects such as carbon-metal boundaries and phase boundaries introduced by the rapid thermal shock. These interfaces promote localized charge accumulation and contribute significantly to interfacial polarization under alternating electromagnetic fields.

The EMA performance of a material is typically characterized by the minimum reflection loss (RL) and effective absorption bandwidth (EAB). The RL at a given frequency is defined by the following equation:

$$RL = 20\log_{10}\frac{|Z_{in} - Z_0|}{|Z_{in} + Z_0|} \tag{1}$$

where Z_0 is the impedance of free space (377 Ω), and Z_{in} is the impedance of the material, which can be calculated from the material's complex permittivity and permeability. The material's complex impedance is given by:

$$Z_{in} = Z_0\sqrt{\frac{\mu_r}{\varepsilon_r}}\tanh\left(j\frac{2\pi f}{c}d\sqrt{\mu_r\varepsilon_r}\right) \tag{2}$$

$$\mu_r = \mu' - j\mu'', \varepsilon_r = \varepsilon' - j\varepsilon'' \tag{3}$$

where μ_r and ε_r are the complex permeability and permittivity of the

material, respectively, f is the frequency of the incident electromagnetic wave, c is the speed of light in a vacuum, and d is the absorber thickness. The EAB is defined as the frequency range where the RL is below a specified threshold (usually −10 dB), indicating effective absorption of electromagnetic waves by the material.

The EMA performance of the Co/C composite was assessed using the coaxial ring method at a fixed filler loading of 15 wt% (Fig. S5). As shown in Fig. 4, the absorption behavior exhibits strong dependence on the thermal treatment strategy. Co-PPc shows negligible absorption, with no EAB and a minimal RL of −2.33 dB at 5.0 mm (Fig. 4a–d). In contrast, Co/C–C delivers a marked enhancement, achieving an EAB of 5.0 GHz and an RL of −34.42 dB at a reduced thickness of 1.43 mm (Fig. 4b–e). The FJH-treated sample achieves the broadest EAB of 6.12 GHz (a 22.4 % increase compared to Co/C–C) and maintains a strong RL of −28.10 dB at 2.15 mm (Fig. 4c–f). These results clearly demonstrate that the application of FJH is highly effective in broadening the absorption bandwidth and enhancing overall EMA performance.

The reflection loss values of all samples were further analyzed across a range of thicknesses (Fig. 4g). Co-PPc exhibits no effective absorption, with all RL values remaining above −10 dB. In contrast, both Co/C–C and Co/C–F demonstrate strong absorption within the 1.5–4.0 mm thickness range. Co/C–C achieves RL values from −27.92 to −10.88 dB, while Co/C–F ranges from −27.42 to −10.59 dB. Overall, the RL magnitudes are comparable between the two samples. These results indicate that FJH treatment does not significantly change the absorption intensity, but contributes to broadening the effective absorption range. In comparison to representative absorbers reported in previous studies [11, 12,43–49], Co/C–F offers a broader frequency coverage (Fig. 4h). The EAB spans from 11.88 to 18.00 GHz, fully covering the Ku-band and partially extending into the upper X-band. This broad working range meets the practical demands of wideband microwave absorption and makes Co/C–F a highly competitive material.

For further analysis, the attenuation of electromagnetic waves in materials is primarily attributed to dielectric loss and magnetic loss (Fig. 5 and S6). Dielectric loss mainly arises from conductive loss and polarization mechanisms, such as dipolar and interfacial polarization. To investigate the dielectric behavior of the Co/C materials, the complex permittivity ($\varepsilon_r = \varepsilon' - j\varepsilon''$) was measured in the frequency range of 2–18 GHz (Fig. 5a). The real part ε' reflects the material's polarization capacity, while the imaginary part ε'' indicates dielectric loss. Co-PPc exhibits the weakest dielectric properties, with ε' around 2.4 and ε'' below 0.1 across the entire frequency range, indicating poor polarization and loss ability. After carbonization and FJH treatment, the ε_r shows a notable enhancement. When comparing, the ε' of Co/C–F is higher in the low-frequency region (2.0–4.68 GHz) and in the high-frequency region (11.68–18.00 GHz), whereas Co/C–C shows higher ε' in the mid-frequency region (4.68–11.68 GHz). For ε'', Co/C–C generally exhibits higher values than Co/C–F across 2–18 GHz, except within a narrow frequency band from 4.80 to 7.12 GHz, where Co/C–F slightly exceeds Co/C–C. These results indicate that FJH treatment enhances the high-frequency polarization ability of Co/C–F, while keeping dielectric loss moderate, which contributes to its broad and stable absorption performance. The dielectric loss factor $\tan\delta_\varepsilon$ ($\tan\delta_\varepsilon = \varepsilon''/\varepsilon'$) reflects the material's dielectric loss capability. As shown in Fig. 5b, Co-PPc maintains low and stable $\tan\delta_\varepsilon$ values across the entire frequency range, indicating weak conductive loss. After carbonization, Co/C–C exhibits improved dielectric loss, with values fluctuating slightly around 0.64. In contrast, Co/C–F shows a more pronounced fluctuation around 0.51, and exceeds Co/C–C only in the 4.80–7.12 GHz range. These results indicate that FJH treatment suppresses overall dielectric loss while increasing its frequency sensitivity. Given that dielectric loss is partially governed by electrical conductivity, a comparison of DC conductivity was conducted, as shown in Fig. 5c. With increasing pressure, all three samples exhibited a rising trend in conductivity. Co-PPc consistently maintained extremely low conductivity, indicating an almost insulating nature. After carbonization, the conductivity increased significantly, reaching 2.8, 3.4, 3.8, and 4.0 S/cm at 10, 15, 20, and 25 MPa. Upon further FJH treatment, the conductivity exhibited an additional increase, with corresponding values of 3.0, 3.9, 4.5, and 5.2 S/cm at the same pressures, reflecting enhanced charge carrier mobility and improved electrical pathways. Polarization relaxation is a key factor influencing the dielectric loss of materials, primarily comprising interfacial polarization and dipole polarization. According to Debye relaxation theory, the ε' and ε'' can be expressed as:

$$\left(\varepsilon' - \frac{\varepsilon_s + \varepsilon_\infty}{2}\right)^2 + (\varepsilon'')^2 = \left(\frac{\varepsilon_s - \varepsilon_\infty}{2}\right)^2 \quad (4)$$

where ε_s and ε_∞ are the static and high frequency permittivity, respectively. To evaluate this behavior, Cole-Cole plots were constructed for Co/C–C and Co/C–F, as shown in Fig. 5d and e. The Cole–Cole plots reveal distinct polarization behaviors in Co/C–C and Co/C–F. For Co/C–C, the distorted semicircle with an extended linear tail suggests the coexistence of multiple dielectric relaxation processes. This pronounced tail is indicative of overlapping dipolar and interfacial polarization mechanisms, associated with structural defects and residual polar groups (N, O) introduced during carbonization. In contrast, Co/C–F exhibits a more compact and semicircular profile, resembling a near-Debye relaxation behavior. This change reflects the suppression of dipolar polarization due to further graphitization by FJH, which eliminates polar functional groups. However, the slight deviation from an ideal semicircle in Co/C–F can be attributed to the presence of interfacial defects, as supported by the enhanced EPR response.

The complex permeability ($\mu_r = \mu' - j\mu''$) characterizes magnetic response and magnetic loss of materials. As shown in Fig. 5f, the μ' of all three samples fluctuates slightly around 1.1. However, the imaginary part, which reflects magnetic loss, shows a notable divergence. For Co/C–C, μ'' remains low and becomes negative beyond 5.6 GHz, suggesting an absence of effective magnetic loss within the measured frequency range. In contrast, after FJH treatment the sample exhibits only a narrow region of negative μ'' (5.96–6.60 GHz) and develops a broad peak spanning 6.24–15.72 GHz. In the high-frequency region, the appearance of negative μ'' may result from the radiation of excess magnetic energy. When the incident electromagnetic wave interacts with the material, it induces currents and generates an alternating magnetic field. If the intensity of this induced magnetic field surpasses that of the original applied magnetic field, a portion of the magnetic energy cannot be effectively dissipated and instead radiates outward, leading to a negative μ'' [50]. This enhancement implies that FJH treatment effectively activates or strengthens high frequency magnetic loss mechanisms. The magnetic loss performance can be assessed by $\tan\delta_\mu$ ($\tan\delta_\mu = \mu''/\mu'$), which reflects the efficiency of magnetic loss. As shown in Fig. 5g, Co-PPc exhibits a low and relatively stable $\tan\delta_\mu$ (−0.03 to 0.14), indicating weak magnetic loss. After carbonization, Co/C–C shows a further decline, with negative values dominating the 2–18 GHz range, suggesting ineffective magnetic dissipation. In contrast, the FJH-treated sample displays a broad and pronounced $\tan\delta_\mu$ peak from 6.24 to 15.72 GHz, confirming the activation of magnetic loss mechanisms, resulted by the formation of resonant Co nanodomains. Notably, this magnetic peak aligns with the valley in $\tan\delta_\varepsilon$, highlighting a complementary interplay between dielectric and magnetic losses that contributes to more balanced and broadband electromagnetic wave absorption. As shown in Fig. 5h, Co-PPc exhibits the lowest saturation magnetization ($M_s = 0.67$ emu/g) and hysteresis loop ($E_h = 0.03$ J), indicating minimal hysteresis loss and reduced energy dissipation. This low M_s value is associated with weak magnetic properties, as evidenced by the very low residual magnetization ($M_r = 0.002$ emu/g) and coercivity ($H_c = 0.0193$ kOe), suggesting that Co-PPc is easily magnetized and demagnetized, with limited ability to retain magnetization. Co/C–C, which underwent the 800 °C tube furnace treatment, shows the highest M_s (6.93 emu/g) and E_h (1.69 J), reflecting the strongest hysteresis loss and

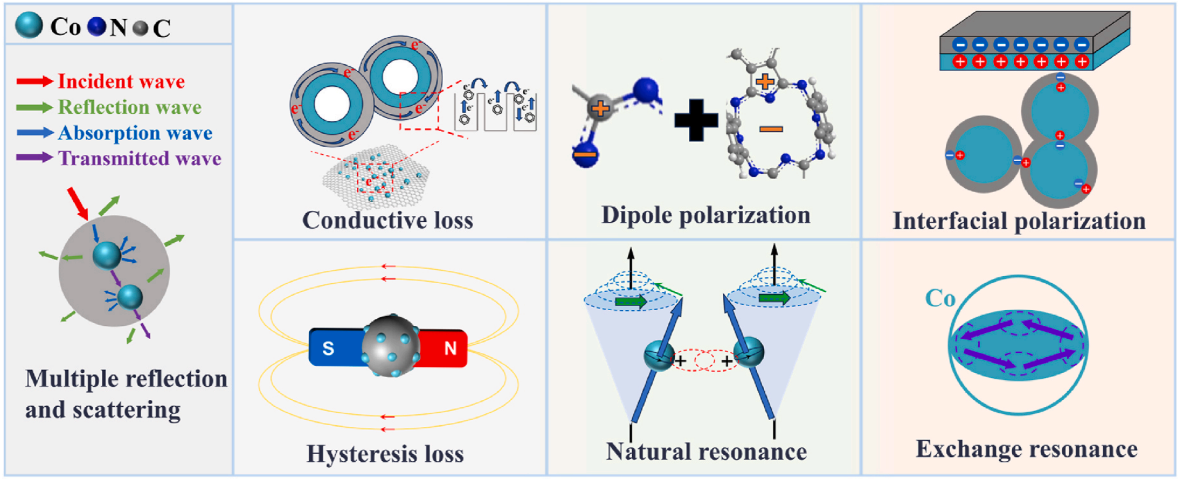

Fig. 6. The illustration diagram of EMW absorption mechanism of Co/C nanocomposite.

a higher energy dissipation. The M_r (0.141 emu/g) and H_c (0.0648 kOe) indicates that this sample maintains a substantial amount of magnetization after the external field is removed. After undergoing FJH treatment, Co/C–F exhibits an intermediate M_s value (3.28 emu/g) and E_h (0.54 J). The M_r (0.044 emu/g) and H_c (0.0449 kOe) of Co/C–F are also intermediate. Therefore, Co/C–F shows a significant decrease in performance compared to Co/C–C after FJH treatment. In terms of eddy current loss (C_0), which expressed as:

$$C_0 = \mu''(\mu')^{-2}f^{-1} = 2\pi\mu_0 d^2\delta \quad (5)$$

where μ_0 is the permeability of free space, d represents a characteristic length of the material, δ is the skin depth. The coefficient C_0 reflects the eddy current loss capability of the material, and its variation trend can be used to determine the dominant magnetic loss mechanism. From Fig. 5i, it indicates that C_0 for Co-PPc remains stable across the entire frequency range but exhibits weak loss capability. In contrast, after carbonization at 800 °C, Co/C–C shows multiple peaks in the 2.12–6.04 GHz range, indicating natural resonance behavior. However, C_0 values for Co/C–C decrease dramatically in the high-frequency region. Further comparison reveals that Co/C–F exhibits multiple fluctuating peaks in the 2.72–6.24 GHz range due to natural resonance. More significantly, Co/C–F displays a prominent broad peak accompanied by smaller peaks in the 6.24–17.64 GHz range, which can be attributed to exchange resonance, with eddy current contributions being negligible [51]. These findings demonstrate that FJH treatment effectively optimizes the magnetic loss mechanism by introducing exchange resonance at higher frequencies, significantly enhancing the broadband electromagnetic wave absorption performance of Co/C–F.

Fig. 6 illustrates the EMW absorption mechanism in the Co/C nanocomposite. Multiple scattering occurs at Co/C interfaces, and heterogeneous carbon regions, prolonging wave propagation paths and enhancing EMW attenuation. Conductive loss stems from charge transport along the carbon network, while dipolar polarization arises from polar groups and Co–N coordination. Interfacial polarization occurs at boundaries between Co nanoparticles and the carbon matrix. Magnetic loss involves hysteresis from domain motion, natural resonance from nanoscale Co domains, and exchange resonance. In Co/C–C, dielectric loss dominates through dipolar and interfacial polarization, while magnetic loss remains weak due to limited Co domain motion and limited natural resonance. After FJH treatment, Co/C–F maintains effective dielectric loss through improved conductivity and rich interfaces, despite reduced dipolar contribution. Meanwhile, magnetic loss is significantly enhanced due to natural resonance and activated exchange resonance, despite substantially reduced hysteresis loss. These results indicate that FJH enables a synergistic combination of dielectric and magnetic losses in Co/C–F, leading to broader and more stable absorption performance.

4. Conclusion

In this work, a 2D Co/C nanocomposite was synthesized from Co-PPc precursors through tube furnace carbonization followed by FJH treatment. Characterizations including TEM, XRD, Raman, and XPS confirm that the FJH process significantly enhances graphitization, improves carbon ordering, and promotes uniform distribution and crystallinity of Co nanoparticles. Compared to the untreated sample, the FJH-treated composite exhibits a 22.4 % increase in effective absorption bandwidth (from 5.0 to 6.12 GHz), along with a strong reflection loss of −28.1 dB. The enhanced electromagnetic wave absorption performance originates from a synergistic effect of mechanisms including conductive loss, interfacial polarization, natural resonance, and activated exchange resonance. These results demonstrate that FJH is a rapid and efficient strategy for tuning microstructure and optimizing broadband electromagnetic absorption behavior in carbon-based nanocomposites.

CRediT authorship contribution statement

Tiancong Hao: Writing – original draft, Methodology, Investigation, Formal analysis. **Yuhang Liu:** Writing – original draft, Methodology, Investigation, Formal analysis. **Wenyu Li:** Software, Investigation, Formal analysis. **Xiaoning Yang:** Writing – review & editing, Visualization, Formal analysis. **Xiongfei Liu:** Visualization, Software, Formal analysis. **Qingya Sun:** Visualization, Validation, Supervision, Project administration, Funding acquisition. **Shifei Tao:** Visualization, Software, Resources. **Aming Xie:** Writing – review & editing, Supervision, Project administration, Funding acquisition, Data curation, Conceptualization. **Guowei Ma:** Writing – review & editing, Supervision.

Data availability statement

The data used to support the findings of this study are available from the corresponding author upon request.

Declaration of competing interest

The authors declare that they have no known competing financial interests or personal relationships that could have appeared to influence the work reported in this paper.

Acknowledgments

This work was supported by the National Natural Science Foundation of China (Grant No. 52273267), and the Fundamental Research Funds for the Central Universities (No.30923011009, 309231C8801).

Appendix A. Supplementary data

Supplementary data to this article can be found online at https://doi.org/10.1016/j.carbon.2025.120593.

References

[1] Y. Ma, R. Liu, L. Sun, S. Wei, X. Li, Progress on microwave absorption performance of carbon fiber reinforced composites, ChemistrySelect 9 (2024) 21–23, https://doi.org/10.1002/slct.202305226.
[2] S. Guo, Y. Bao, Y. Li, H. Guan, D. Lei, T. Zhao, B. Zhong, Z. Li, Super broadband absorbing hierarchical CoFe alloy porous carbon@carbon nanotubes nanocomposites derived from metal-organic frameworks, J. Mater. Sci. Technol. 118 (2022) 218–228, https://doi.org/10.1016/j.jmst.2021.11.054.
[3] W. Liu, S. Tan, Z. Yang, G. Ji, Hollow graphite spheres embedded in porous amorphous carbon matrices as lightweight and low-frequency microwave absorbing material through modulating dielectric loss, Carbon 138 (2018) 143–153, https://doi.org/10.1016/j.carbon.2018.06.009.
[4] C. Liu, J. Qiao, X. Zhang, D. Xu, N. Wu, L. Lv, W. Liu, J. Liu, MOF-derived porous CoNi/C nanocomposites with ultra-wide band microwave absorption properties, New J. Chem. 43 (2019) 16546–16554. https://doi/10.1021/acsami.5b03177.
[5] L. Liang, Q. Li, X. Yan, Y. Feng, Y. Wang, H. Zhang, X. Zhou, C. Liu, C. Shen, X. Xie, Multifunctional magnetic $Ti_3C_2T_X$ MXene/Graphene aerogel with superior electromagnetic wave absorption performance, Angew. Chem., Int. Ed. 15 (2021) 6622–6632. https://doi/10.1021/acsnano.0c09982.
[6] J. Chai, J. Cheng, D. Zhang, Y. Xiong, X. Yang, X. Ba, S. Ullah, G. Zheng, M. Yan, M. Cao, Enhancing electromagnetic wave absorption performance of Co_3O_4 nanoparticles functionalized MoS_2 nanosheets, J. Alloys Compd. 829 (2020) 154531. https://dx.doi.org/10.1016/j.jallcom.2020.154531.
[7] H. Zhang, J. Cheng, H. Wang, Z. Huang, Q. Zheng, G. Zheng, D. Zhang, R. Che, M. Cao, Initiating VB-Group laminated NbS_2 electromagnetic wave absorber toward superior absorption bandwidth as large as 6.48 GHz through phase engineering modulation, Adv. Funct. Mater. 32 (2022) 2108194, https://doi.org/10.1002/adfm.202108194.
[8] X. Zheng, Z. Tian, R. Bouchal, M. Antonietti, N. López-Salas, M. Odziomek, Tin (II) chloride salt melts as non-innocent solvents for the synthesis of low-temperature nanoporous Oxo-carbons for nitrate electrochemical hydrogenation, Adv. Mater. 36 (2023) 16, https://doi.org/10.1002/adma.202311575.
[9] X. Su, J. Wang, T. Liu, Y. Zhang, Y. Liu, B. Zhang, Y. Liu, H. Wu, H. Xu, Controllable atomic migration in microstructures and defects for electromagnetic wave absorption enhancement, Adv. Funct. Mater. 34 (2024) 39, https://doi.org/10.1002/adfm.202403397.
[10] Z. Xu, Y. Du, D. Liu, Y. Wang, W. Ma, Y. Wang, P. Xu, X. Han, Pea-like Fe/Fe_3C nanoparticles embedded in nitrogen-doped carbon nanotubes with tunable dielectric/magnetic loss and efficient electromagnetic absorption, ACS Appl. Mater. Interfaces 11 (2019) 4268–4277. https://doi/10.1021/acsami.8b19201.
[11] L. Yang, H. Lv, M. Li, Y. zhang, J. Liu, Z. Yang, Multiple polarization effect of shell evolution on hierarchical hollow C@MnO_2 composites and their wideband electromagnetic wave absorption properties, Chem. Eng. J. 392 (2020) 123666, https://doi.org/10.1016/j.cej.2019.123666.
[12] Y. Lu, Y. Wang, H. Li, Y. Lin, Z. Jiang, Z. Xie, Q. Kuang, L. Zheng, MOF-derived porous Co/C nanocomposites with excellent electromagnetic wave absorption properties, ACS Appl. Mater. Interfaces 7 (2015) 13604–13611. https://doi/10.1021/acsami.5b03177.
[13] J. Xu, Z. Ma, P. Yang, C. Zhu, Y. Chen, 3D hierarchically ordered porous carbon frameworks/Co nanoparticles for broadening electromagnetic wave absorption bandwidth, Carbon 233 (2025) 119916, https://doi.org/10.1016/j.carbon.2024.119916.
[14] Y. Shen, Z. Ma, F. Yan, C. Zhu, X. Zhang, Y. Chen, Enhanced interfacial polarization loss of FeS/MoS_2@N-Doped carbon sandwich-walled nanotubes enables high-performance electromagnetic wave absorption, Adv. Funct. Mater. 1616 (2025) 2423947, https://doi.org/10.1002/adfm.202423947.
[15] J. Su, X. Zhang, Z. Ma, X. Xu, J. Xu, Y. Chen, Construction of Fe_3C@N-doped graphene layers yolk-shelled nanoparticles on the graphene sheets for high-efficient electromagnetic wave absorption, Carbon 229 (2024) 119448, https://doi.org/10.1016/j.carbon.2024.119448.
[16] L. Gai, H. Zhao, X. Li, P. Wang, S. Yu, Y. Chen, C. Wang, D. Lan, F. Han, Y. Du, Shell engineering afforded dielectric polarization prevails and impedance amelioration toward electromagnetic wave absorption enhancement in nested-network carbon architecture, Chem. Eng. J. 501 (2024) 157645, https://doi.org/10.1016/j.cej.2024.157556.
[17] D. Cai, D. Wang, B. Liu, Y. Wang, Y. Liu, L. Wang, H. Li, H. Huang, Q. Li, T. Wang, A comparison of the electrochemical performance of graphitized coal prepared by high-temperature heating and flash Joule heating as an anode material for lithium and potassium ion batteries, Chem. Phys. Lett. 815 (2023) 140362. https://doi/10.1016/j.cplett.2023.140362.
[18] S. Peng, S. Wang, G. Hao, C. Zhu, Y. Zhang, X. Lv, Y. Hu, W. Jiang, Preparation of magnetic flower-like carbon-matrix composites with efficient electromagnetic wave absorption properties by carbonization of MIL-101(Fe), J. Magn. Magn Mater. 487 (2019) 165306, https://doi.org/10.1016/j.jmmm.2019.165306.
[19] K. Zhang, A. Xie, M. Sun, W. Jiang, F. Wu, W. Dong, Electromagnetic dissipation on the surface of metal organic framework (MOF)/reduced graphene oxide (RGO) hybrids, Mater. Chem. Phys. 199 (2017) 340–347, https://doi.org/10.1016/j.matchemphys.2017.07.026.
[20] H. Zhao, F. Wang, L. Cui, X. Xu, X. Han, Y. Du, Composition optimization and microstructure design in MOFs-Derived magnetic carbon-based microwave absorbers: a review, Nano-Micro Lett. 13 (2021) 208, https://doi.org/10.1007/s40820-021-00734-z.
[21] Y. Wang, X. Li, X. Han, P. Xu, L. Cui, H. Zhao, D. Liu, F. Wang, Y. Du, Ternary Mo_2C/Co/C composites with enhanced electromagnetic waves absorption, Chem. Eng. J. 387 (2020) 19, https://doi.org/10.1016/j.cej.2020.124159.
[22] X. Chen, J. Zhou, Z. Xiao, T. Han, Y. Zhou, Q. Chen, W. Tang, Promoting reaction kinetics of lithium polysulfides by cobalt polyphthalocyanine derived ultrafine Co nanoparticles mono-dispersed on graphene flakes for Li-S batteries, J. Cent. South Univ. 29 (2022) 2940–2955. https://doi/10.1007/s11771-022-5134-2.
[23] Y. Bhattacharjee, S. Bose, Core-shell nanomaterials for microwave absorption and electromagnetic interference shielding: a review, ACS Appl. Nano Mater. 4 (2021) 949–972. https://pubs.acs.org/doi/10.1021/acsanm.1c00278.
[24] Y. Fang, Y. Liu, L. Qi, Y. Xue, Y. Li, 2D graphdiyne: an emerging carbon material, chemical society reviews 51, Chem. Soc. Rev. 1 (2022) 2681–2709. https://doi/10.1039/D1CS00592H.
[25] Y. Liu, F. Wang, Y. Wang, B. Hu, P. Xu, X. Han, Y. Du, A combined engineering of hollow and core-shell structures for C@MoS_2 microcapsules toward high-efficiency electromagnetic absorption, Composites, Part B 273 (2024) 111244, https://doi.org/10.1016/j.compositesb.2024.111244.
[26] L. Eddy, S. Xu, C. Liu, P. Scotland, W. Chen, J. Beckham, B. Damasceno, C. Choi, K. Silva, A. Lathem, Y. Han, B. Yakobson, X. Zhang, Y. Zhao, J. Tour, Electric field effects in flash Joule heating synthesis, J. Am. Chem. Soc. 146 (2024) 16010–16019. https://doi/10.1021/jacs.4c02864.
[27] Q. Dong, Y. Yao, S. Cheng, K. Alexopoulos, J. Gao, S. Srinivas, Y. Wang, Y. Pei, C. Zheng, A. Brozena, H. Zhao, X. Wang, H. Toraman, B. Yang, I. Kevrekidis, Y. Ju, D. Vlachos, D. Liu, L. Hu, Programmable heating and quenching for efficient thermochemical synthesis, Nature 605 (2022) 470–476, https://doi.org/10.1038/s41586-022-04568-6.
[28] X. Wang, Y. Zhao, G. Chen, X. Zhao, C. Liu, S. Sridar, S. Li, A. Brozena, M. Guo, H. Zhang, Y. Wang, W. Xiong, L. Hu, Ultrahigh-temperature melt printing of multi-principal element alloys, Nat. Commun. 13 (2022) 6724, https://doi.org/10.1038/s41467-022-34471-7.
[29] H. Xie, N. Liu, Q. Zhang, H. Zhong, L. Guo, X. Zhao, D. Li, S. Liu, Z. Huang, A. Lele, A. Brozena, X. Wang, K. Song, S. Chen, Y. Yao, M. Chi, W. Xiong, J. Rao, M. Zhao, M. Shneider, J. Luo, J. Zhao, Y. Ju, L. Hu, A stable atmospheric-pressure plasma for extreme-temperature synthesis, Nature 623 (2023) 964–971, https://doi.org/10.1038/s41586-023-06694-1.
[30] Q. Dong, A. Lele, X. Zhao, S. Li, S. Cheng, Y. Wang, M. Cui, M. Guo, A. Brozena, Y. Lin, T. Li, L. Xu, A. Qi, I. Kevrekidis, J. Mei, X. Pan, D. Liu, Y. Ju, L. Hu, Depolymerization of plastics by means of electrified spatiotemporal heating, Nature 616 (2023) 488–494, https://doi.org/10.1038/s41586-023-05845-8.
[31] Z. Huang, T. Li, B. Li, Q. Dong, J. Smith, S. Li, L. Xu, G. Wang, M. Chi, L. Hu, Tailoring local chemical ordering via elemental tuning in high-entropy alloys, J. Am. Chem. Soc. 146 (2024) 2167–2173. https://doi/10.1021/jacs.3c12048.
[32] Y. Mao, P. Ma, T. Li, H. Liu, X. Zhao, S. Liu, X. Jia, S. Rahaman, X. Wang, M. Zhao, G. Chen, H. Xie, A. Brozena, B. Zhou, Y. Luo, R. Tarté, C.-I. Wei, Q. Wang, R. Briber, L. Hu, Flash heating process for efficient meat preservation, Nat. Commun. 15 (2024) 3893, https://doi.org/10.1038/s41467-024-47967-1.
[33] X. Wang, Y. Zhao, G. Chen, X. Zhao, C. Liu, S. Sridar, L. Pizano, S. Li, A. Brozena, M. Guo, H. Zhang, Y. Wang, W. Xiong, L. Hu, Ultrahigh-temperature melt printing of multi-principal element alloys, Nat. Commun. 13 (2022) 1, https://doi.org/10.1038/s41467-022-34471-7.
[34] F. Wang, Y. Liu, R. Feng, X. Wang, X. Han, Y. Du, A "Win-Win" strategy to modify Co/C foam with carbon microspheres for enhanced dielectric loss and microwave absorption characteristics, Small 19 (48) (2023) 2303597, https://doi.org/10.1002/smll.202303597.
[35] Y. Jiao, Z. Dai, M. Feng, J. Luo, Y. Xu, Electromagnetic absorption behavior regulation in bimetallic polyphthalocyanine derived CoFe-alloy/C 0D/2D nanocomposites, Mater. Today Phys. 33 (2023) 101058, https://doi.org/10.1016/j.mtphys.2023.101058.
[36] Q. Qi, J. Hu, S. Guo, H. Song, S. Wang, Y. Yao, T. Le, W. Li, C. Zhang, L. Zhang, Large-scale synthesis of low-cost bimetallic polyphthalocyanine for highly stable water oxidation, Appl. Catal. B Environ. 299 (2021) 120637, https://doi.org/10.1016/j.apcatb.2021.120637.
[37] M. Hao, Z. Hu, Y. Huang, X. Qian, Z. Wen, X. Wang, L. Liu, F. Lu, Y. Zhang, Enhanced both in-plane and through-thickness thermal conductivity of carbon fiber/epoxy composites by fabricating high thermal conductive coaxial PAN/PBO carbon fibers, Composites, Part B 229 (2022) 109468, https://doi.org/10.1016/j.compositesb.2021.109468.
[38] J. Tao, Z. Jiao, L. Xu, P. Yi, Z. Yao, F. Yang, C. Zhou, P. Chen, J. Zhou, Z. Li, Construction of MOF-derived Co/C shell on carbon fiber surface to enhance multi-polarization effect towards efficient broadband electromagnetic wave absorption, Carbon 184 (2021) 571–582, https://doi.org/10.1016/j.carbon.2021.08.064.
[39] Y. Bi, M. Ma, Y. Liu, Z. Tong, R. Wang, K. Chung, A. Ma, G. Wu, Y. Ma, C. He, P. Liu, L. Hu, Microwave absorption enhancement of 2-dimensional CoZn/C@

MoS_2@PPy composites derived from metal-organic framework, J. Colloid Interface Sci. 600 (2021) 209–218, https://doi.org/10.1016/j.jcis.2021.04.137.
[40] P. Yin, L. Zhang, Y. Tang, J. Liu, Earthworm-like (Co/CoO)@C composite derived from MOF for solving the problem of low-frequency microwave radiation, J. Alloys Compd. 881 (2021) 160556, https://doi.org/10.1016/j.jallcom.2021.160556.
[41] X. Wang, L. Zhang, N. Wang, S. Sun, H. Wan, R. Ma, W. Ma, Boosting electrocatalytic oxygen reduction of Fe-Co polyphthalocyanine via the synergy of metal component optimization and axial ligand modification, Chem. Eng. J. 499 (2024) 156609, https://doi.org/10.1016/j.cej.2024.156609.
[42] Y. Wang, Y. Pan, X. Zhang, X. Huang, T. Li, S. Liu, S. Tang, Y. Sun, B. Shao, Z. Liu, Defect engineering boosting PMS activation activity on cobalt polyphthalocyanine: promoting Co(IV)=O formation and enhancing $^1O_2$ selectivity, Sep. Purif. Technol. 357 (2025) 130085, https://doi.org/10.1016/j.seppur.2024.130085.
[43] A. Xie, D. Sheng, W. Liu, Y. Chen, S. Cheng, Enhancing electromagnetic absorption performance of molybdate@carbon by metal ion substitution, J. Mater. Sci. Technol. 163 (2023) 92–100, https://doi.org/10.1016/j.jmst.2023.05.004.
[44] R. Shu, W. Li, Y. Wu, J. Zhang, G. Zhang, Nitrogen-doped Co-C/MWCNTs nanocomposites derived from bimetallic metal–organic frameworks for electromagnetic wave absorption in the X-band, Chem. Eng. J. 362 (2019) 513–524, https://doi.org/10.1016/j.cej.2019.01.090.
[45] C. Li, Y. Ge, X. Jiang, Z. Zhang, L. Yu, The rambutan-like C@$NiCo_2O_4$ composites for enhanced microwave absorption performance, J. Mater. Sci. Mater. Electron. 30 (2019) 3124–3136, https://doi.org/10.1007/s10854-018-00592-3.
[46] X. Xiao, W. zhu, Z. Tan, W. Tian, Y. Guo, H. Wang, J. Fu, X. Jian, Ultra-small Co/CNTs nanohybrid from metal organic framework with highly efficient microwave absorption, Composites, Part B 152 (2018) 316–323, https://doi.org/10.1016/j.compositesb.2018.08.109.
[47] C. Fu, D. He, Y. Wang, X. Zhao, Enhanced microwave absorption properties of polyaniline-modified porous Fe_3O_4@C nanosheets, J. Mater. Sci. Mater. Electron. 30 (2019) 11907–11913, https://doi.org/10.1007/s10854-019-01528-1.
[48] M. Sun, D. Wang, Z. Xiong, Z. Zhang, L. Qin, C. Chen, F. Wu, P. Liu, Multi-dimensional Ni@C-CoNi composites with strong magnetic interaction toward superior microwave absorption, J. Mater. Sci. Technol. 130 (2022) 176–183, https://doi.org/10.1016/j.jmst.2022.05.016.
[49] S. Mathan, M. Selvaraj, M. Assiri, K. Kandiah, R. Rajendran, Synthetic nanoarchitectonics with ultrafast Joule heating of graphene-based electrodes for high energy density supercapacitor application, Surf. Interface Anal. 51 (2024) 104707, https://doi.org/10.1016/j.surfin.2024.104707.
[50] L. Yao, J. Zhao, Y. Wang, M. Cao, Manipulating electromagnetic response for tunable microwave absorption, electromagnetic interference shielding, and device, Carbon 212 (2023) 118169, https://doi.org/10.1016/j.carbon.2023.118169.
[51] B. Dai, Y. Ma, F. Dong, J. Yu, M. Ma, H. Thabet, S. El-Bahy, M. Ibrahim, M. Huang, I. Seok, G. Roymahapatra, N. Naik, B. Xu, J. Ding, T. Li, Overview of MXene and conducting polymer matrix composites for electromagnetic wave absorption, Adv. Compos. Hybrid Mater. 5 (2022) 704–754, https://doi.org/10.1007/s42114-022-00510-6.